

Article

Accelerated Decoloration of Organic Dyes from Wastewater Using Ternary Metal/g-C₃N₄/ZnO Nanocomposites: An Investigation of Impact of g-C₃N₄ Concentration and Ni and Mn Doping

Muhammad Azam Qamar ^{1,*}, Sammia Shahid ¹, Mohsin Javed ¹, Mohammad Shariq ^{2,*},
Mohammed M. Fadhali ^{2,3}, Osama Madkhali ², Syed Kashif Ali ⁴, Imam Saheb Syed ⁴, Majed Yusef Awaji ^{2,5},
Mohd. Shakir Khan ^{6,*}, Dalin A. Hassan ⁷ and M. Hisham Al Nasir ⁸

¹ Department of Chemistry, School of Science, University of Management and Technology, Lahore 54770, Pakistan

² Department of Physics, College of Science, Jazan University, Jazan 45142, Saudi Arabia

³ Department of Physics, Faculty of Science, Ibb University, Ibb 70270, Yemen

⁴ Department of Chemistry, College of Science, Jazan University, Jazan 45142, Saudi Arabia

⁵ UMR CNRS 7198, Institute Jean Lamour, University of Lorraine, 54011 Nancy, France

⁶ Department of Physics, College of Science, Al-Zulfi, Majmaah University, Al-Majmaah 11952, Saudi Arabia

⁷ Department of Pharmacology and Toxicology, College of Pharmacy, Jazan University, Jazan 45142, Saudi Arabia

⁸ Department of Applied Physics, Federal Urdu University of Arts Science and Technology, Islamabad 44000, Pakistan

* Correspondence: qamariub@gmail.com (M.A.Q.); mohammadshariq@jazanu.edu.sa (M.S.); ms.khan@mu.edu.sa (M.S.K.)



Citation: Qamar, M.A.; Shahid, S.; Javed, M.; Shariq, M.; Fadhali, M.M.; Madkhali, O.; Ali, S.K.; Syed, I.S.; Awaji, M.Y.; Shakir Khan, M.; et al. Accelerated Decoloration of Organic Dyes from Wastewater Using Ternary Metal/g-C₃N₄/ZnO Nanocomposites: An Investigation of Impact of g-C₃N₄ Concentration and Ni and Mn Doping. *Catalysts* **2022**, *12*, 1388. <https://doi.org/10.3390/catal12111388>

Academic Editor: Da-Ren Hang

Received: 19 September 2022

Accepted: 20 October 2022

Published: 8 November 2022

Publisher's Note: MDPI stays neutral with regard to jurisdictional claims in published maps and institutional affiliations.



Copyright: © 2022 by the authors. Licensee MDPI, Basel, Switzerland. This article is an open access article distributed under the terms and conditions of the Creative Commons Attribution (CC BY) license (<https://creativecommons.org/licenses/by/4.0/>).

Abstract: Wastewater from many sectors that contains hazardous organic pollutants exacerbates environmental contamination. Consequently, outstanding photocatalytic substances that can successfully degrade hazardous substances are needed to provide pollution-free water. From this perspective, zinc oxide/g-C₃N₄-based composites are desirable due to their low cost, strong reactivity, and environmental friendliness. So, in the current investigation, sequences of Mn/g-C₃N₄/ZnO (Mn/GZ) and Ni/g-C₃N₄/ZnO (Ni/GZ) nanocomposites (NCs) containing different concentrations (wt.%) of g-C₃N₄ were made via the co-precipitation process. The chemical makeup and morphological characteristics of the produced composites were ascertained via the techniques of transmission electron microscopy (TEM), scanning electron microscopy (SEM), energy-dispersive X-ray (EDX), Fourier transform infrared (FTIR), photoluminescence (PL), and UV spectrophotometry. Methyl orange (MO) and Eriochrome Black T (EBT) dyes were used as target pollutants to assess the composite materials' photocatalytic effectiveness. Compared to g-C₃N₄/ZnO and g-C₃N₄, the produced Mn/GZ and Ni/GZ NCs displayed better photocatalytic activity. The improved photocatalytic efficiency of the Ni/GZ and Mn/GZ NCs might be credited to synergistic interactions at the g-C₃N₄ and ZnO interface that result in a more efficient separation and conduction of photo-induced charges. Furthermore, the Ni/Mn atoms act as the facilitators to improve electron-hole pair separation and conduction in NCs. The nanocomposites were found to be incredibly stable, with consistently high dye decoloration efficiency over five catalytic cycles. Hence, Ni/GZ and Mn/GZ could potentially be very effective and adaptable photocatalysts for the photocatalytic decoloration of wastewater pollutants.

Keywords: Eriochrome Black T; g-C₃N₄/ZnO; wastewater; hazardous contaminants; nanocomposites

1. Introduction

Our planet is currently in severe environmental jeopardy. Our world's environmental conditions are getting worse due to the industrial pollutants being released into the

ecosystem directly (water, soil, and air). Wastewater contains a variety of contaminants, including pathogenic bacteria, heavy metal ions, organic dyes, and pharmaceuticals [1,2]. Due to increased water demands and diminishing supply, these dangerous substances must be separated from wastewater and kept away from the aquatic environment. During the past two decades, great emphasis has been placed on the photocatalytic removal of organic contaminants using semiconductor materials. This method is based on the formation of reactive oxygen species (ROS) by semiconductor materials when they are exposed to sunlight [3,4]. Numerous semiconductor photocatalysts with various nanostructures have been explored, including TiO₂, ZnO, CuO, NiS, SnO₂, ZrO₂, and WO₃. Due to their large band gaps and quick electron–hole recombination, these photocatalysts are limited in visible-light photocatalysis [4,5].

ZnO is an efficient photocatalyst because of its high yield, stability, affordability, and superior optical characteristics [4,6–8]. Its unusual qualities make it useful in photocatalysis, solar cells, and catalytic processes. However, ZnO's light absorption is primarily restricted to the UV area and is very weakly responsive to visible radiation because of its large E_g value (~3.37 eV) [9,10]. ZnO also has several disadvantages, including the speedy recombination of photogenerated e^-/h^+ pairs, photo corrosion, and visible-light inactivity [11,12]. Because of the fast e^-/h^+ pair recombination, very few electrons are transported to the pollutant's conduction band. These issues pose a practical challenge for using ZnO in photocatalytic processes [13,14]. Many techniques have been emerge to alter its band structure, including doping metal or nonmetal and forming composites with appropriate materials. Doping helps to narrow the band gap by inserting impurities among energy levels in the form of a mid-gap state [15–17]. Thus, the most successful method to solve these issues is the composite creation of ZnO with semiconductors and carbon compounds [17,18].

When exposed to visible light, the $g\text{-C}_3\text{N}_4$ semiconductor demonstrated excellent photocatalytic performance. This is due to its high stability and narrow band gap, which allows it to absorb more visible light. It possesses excellent physical, thermal, optical, and electrical characteristics [19,20]. This highly stable metal-free polymer uses inexpensive starting molecules, including urea, thiourea, and melamine, through a simplistic heating procedure. Compared to inorganic conjugative materials, its softness makes it easier to coat on other materials (like CNTs and graphene) [21,22]. Furthermore, its well-crystallized lamellar structure has a higher affinity for charge transfer than other conjugative organic compounds [23,24]. As a polymeric matrix with a moderate band gap, $g\text{-C}_3\text{N}_4$ can generate hydrogen, split water, and reduce CO₂ [13]. $g\text{-C}_3\text{N}_4$ is an excellent contender for a variety of uses in the visible spectrum range [25]. However, $g\text{-C}_3\text{N}_4$ is not an effective photocatalyst in pure form due to the fast recombination of photoinduced e^-/h^+ pairs [26]. As a result, numerous efforts have been made to get around this restriction, including using vacancies, making heterojunctions, and mixing $g\text{-C}_3\text{N}_4$ with nonmetals and other metal oxides [27].

Integrating $g\text{-C}_3\text{N}_4$ and metal ions with ZnO has been one of the most successful methods for improving ZnO's photocatalytic efficiency. It is reported that ZnO modified with $g\text{-C}_3\text{N}_4$ or doped with a metal ZnO accelerates e^-/h^+ pair transmission and promotes the production of active species [28–30]. Li et al. reported that mesoporous carbon/ $g\text{-C}_3\text{N}_4$ NCs made via a thermal process had improved photocatalytic efficiency against RhB as compared to $g\text{-C}_3\text{N}_4$ [31]. According to Wang et al., Mn- $g\text{-C}_3\text{N}_4$ outperformed pristine $g\text{-C}_3\text{N}_4$ in the photocatalytic diminution of Cr (VI) and degradation of RhB by nearly nine times and six times, respectively [32]. According to the findings of Wang et al., Eu- $g\text{-C}_3\text{N}_4$ demonstrated photocatalytic degradation of RhB that was six times superior to that by $g\text{-C}_3\text{N}_4$ [33]. Similarly, Tonda et al. showed that Fe- $g\text{-C}_3\text{N}_4$ displayed better photocatalytic decoloration of RhB dye in visible wavelengths, as compared to $g\text{-C}_3\text{N}_4$ [34].

In current study, we fabricated metal/ $g\text{-C}_3\text{N}_4$ /ZnO NCs by doping $g\text{-C}_3\text{N}_4$ /ZnO with Ni and Mn metal ions individually to realize significant photocatalytic performance. The metal-doped $g\text{-C}_3\text{N}_4$ /ZnO NCs were fabricated via a surfactant (PEG) assisted precipitation method, and the resulting Ni/ $g\text{-C}_3\text{N}_4$ /ZnO (Ni/GZ) and Mn/ $g\text{-C}_3\text{N}_4$ /ZnO

(Mn/GZ) NCs were used to decompose methyl orange (MO) and Eriochrome Black T (EBT) dyes. EBT and MO are water-soluble azo dyes that cause human ailments. Their removal from water is challenging since they are not destroyed by aerobic or biological oxidation [35,36]. The decoloration results of these dyes can be considered as a model for other organic contaminants/dyes. The photocatalytic decoloration study was carried out in two steps.

In step one, Mn/GZ and Ni/GZ photocatalysts of varying g-C₃N₄ percentages (20, 30, 40, 50, 60, 70, and 80 wt.%) were synthesized. In the current research, the effect of Ni/Mn substitution (3 wt.% for Ni and Mn metal ions, since this is the mainly cited doping amount in the literature) and g-C₃N₄ percentages on the photocatalytic properties of Ni/GZ and Mn/GZ NCs was observed. The Mn (4s²3d⁵) and Ni (4s²3d⁸) metal ions were chosen as dopants because these can be considered as preventative for transition metals (having a filling trend from half-filled d orbital towards complete filling). The Mn/50%g-C₃N₄/ZnO (Mn/50GZ) and Ni/60%g-C₃N₄/ZnO (Ni/60GZ) photocatalysts manifested the maximum decoloration efficiency under solar light. In step two, the comparative photocatalytic efficiency of Ni/60GZ and Mn/50GZ NCs was observed against EBT and MO dyes. The results showed that the photocatalytic activity of Ni/60GZ and Mn/50GZ NCs was increased because of enhanced sunlight absorption and improved separation of e⁻/h⁺ couples. The current investigation proves the usefulness of (Ni/Mn)/g-C₃N₄/ZnO for eliminating contaminants from our environment.

2. Materials and Methods

2.1. Materials

Nickel nitrate (Ni(NO₃)₂·6H₂O) (99.99%), polyethylene glycol (PEG), zinc acetate dihydrate (Zn(CH₃COO)₂·2H₂O) (98%), sodium hydroxide (NaOH) (98%), manganese (II) acetate tetrahydrate ((CH₃COO)₂Mn·4H₂O) (99.99%), Eriochrome Black T (99.99%), methyl orange (99.99%), and urea (CO(NH₂)₂) (99.99%) were bought from Merck Pakistan and which were utilized exactly as received.

2.2. Synthesis of g-C₃N₄

Thermal polycondensation of urea to 570 °C in a muffle furnace for 5 h at 5 °C min⁻¹ produced a yellowish g-C₃N₄ powder [37]. In summary, an alumina crucible containing 5 grams of urea was placed in a muffle furnace. The urea was then calcined for 5 h at 5 °C min⁻¹ at 570 °C to produce light-yellow urea. Before being processed into a finer powder, the final material was cooled to room temperature.

2.3. Synthesis of Composite Nanostructures

A range of targeted Ni/GZ and Mn/GZ NCs with varying g-C₃N₄ percentages (20, 30, 40, 50, 60, 70, and 80 wt.%) were produced via the PEG-assisted chemical coprecipitation method [38]. For the preparation of Ni/20GZ NCs, 0.34 gm of g-C₃N₄, 0.01 M Ni(NO₃)₂·6H₂O, and 0.1 M of Zn(CH₃COO)₂·2H₂O (2.20 g) were placed in a beaker and homogenized in 200 mL of deionized water (D. I). Then, 10 mL of PEG solution was added, and the mixture was stirred on the magnetic stirrer for 1 h. Finally, orange-brown precipitates were obtained by adding 2 M NaOH solution. After filtering off the precipitates, they were rinsed with 100% ethanol and D. I water. The precipitates were then dried at 85 °C and calcinated in an oven at 560 °C for 5 h (5 °C·min⁻¹). The similar method was used to produce Ni/GZ and Mn/GZ NCs containing other percentages (20, 30, 40, 50, 60, 70, and 80 wt.%) of g-C₃N₄; the percentages for different combinations are detailed in Tables S1 and S2. For the synthesis of Mn/GZ NCs, the (CH₃COO)₂Mn·4H₂O salt was used as the Mn precursor, and the remaining steps were the same as detailed for Ni/GZ NCs. g-C₃N₄/ZnO NCs and ZnO NPs were also synthesized for comparative study, as explained by Mudassar et al. [37]. The main steps involved in synthesizing NCs are given in Figure 1.

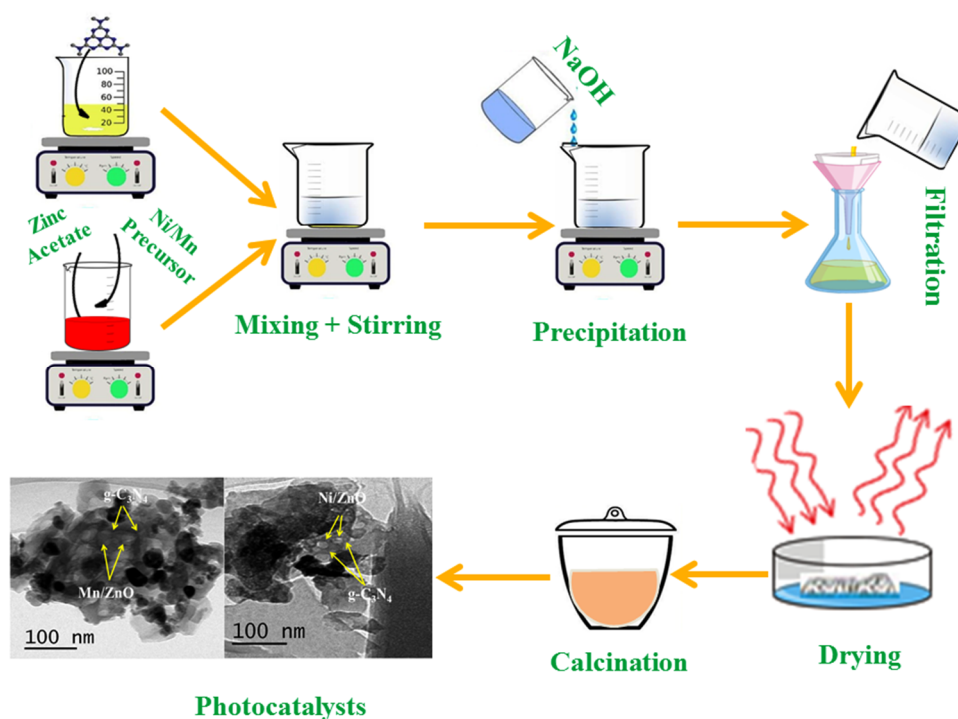


Figure 1. Schematic description of the synthesis of metal/ $g\text{-C}_3\text{N}_4/\text{ZnO}$ nanocomposites.

2.4. Characterization

The Structure of the Produced Materials Was Studied by XRD (Bruker AXS, D8-S4, USA) at 40 kV and 30 mA at Room Temperature with Cu K Radiation ($k = 1.54056$)

The structure of the produced materials was studied by XRD (Bruker AXS, D8-S4, Billerica, MA, USA) at 40 kV and 30 mA at room temperature with Cu K radiation ($k = 1.54056 \text{ \AA}$), while the elemental composition and surface morphology were determined using SEM-EDS (Hitachi, S-4800, Tokyo, Japan). A UV-vis-NIR spectrophotometer was used to analyze the reflectance and photocatalytic absorption spectra (UV-770, Jasco, Tokyo, Japan). The surface morphologies of the photocatalysts were studied using a transmission electron microscope (TEM, JEOL-JEM-1230, Billerica, MA, USA). FT-IR spectrometers with a resolution of 1 cm^{-1} recorded functional groups in the $4000\text{--}400 \text{ cm}^{-1}$ range (Perkin 400 FT-IR, Billerica, MA, USA).

2.5. Photocatalytic Activity

The photocatalyzed dye decoloration activity of each produced photocatalyst was assessed under presence of sunlight. As organic dyes, EBT and MO aqueous solutions were used as the standard contaminants for examining the photocatalytic efficiencies. A quantity of 0.2 g of photocatalyst was diffused in 100 mL of dye solution ($10 \text{ mg}\cdot\text{L}^{-1}$). Each suspension was sonicated for 15 min and then placed in the dark for 30 min to achieve adsorption–desorption equilibrium. After that, the suspension was positioned under solar light ($68\text{--}73 \text{ klux}$) (LT300, Exttech, UK) in an open atmosphere, and aliquots of 5 mL were collected after every 30 min. After centrifugation, a UV-vis spectrophotometer was used to measure the sample's photocatalytic activity. The λ_{max} for EBT was measured at 531 nm, and that for MO was measured at 464 nm [39–41].

3. Results and Discussion

3.1. FTIR Analysis

Figure 2 shows a comparison of the FT-IR spectra of the photocatalysts in the $4000\text{--}450 \text{ cm}^{-1}$ wavenumber band. The observed band at 879 cm^{-1} in the FT-IR spectrum of ZnO confirms the presence of the metal–oxygen bond and the absence of all other functional groups [11]. Stretching of the O–H bond causes the peak at around $3300\text{--}3450 \text{ cm}^{-1}$, while bending of

the O-H bond causes the peak at about 1696 cm^{-1} [11]. The bending at 1504 cm^{-1} is caused by H-O-H vibrations, which suggests that the ZnO NPs absorbed H_2O . A wide-ranging band at 3178 cm^{-1} in the FT-IR spectrum of $\text{g-C}_3\text{N}_4$ appeared due to O-H bond stretching; the peaks in the range $1500\text{--}2000\text{ cm}^{-1}$ are due to the stretching vibrations of C=N, and peaks in the range $1500\text{--}1000\text{ cm}^{-1}$ are due to C-N bond stretching [42]. A peak at 805 cm^{-1} indicates the triazine unit. Also, a band at 2355 cm^{-1} can be accredited to adsorbed carbon dioxide in all the samples [43]. The FT-IR spectra of the Ni/GZ and Mn/GZ composites contain the peaks corresponding to both ZnO and $\text{g-C}_3\text{N}_4$, signifying that the composites were formed successfully [43–45].

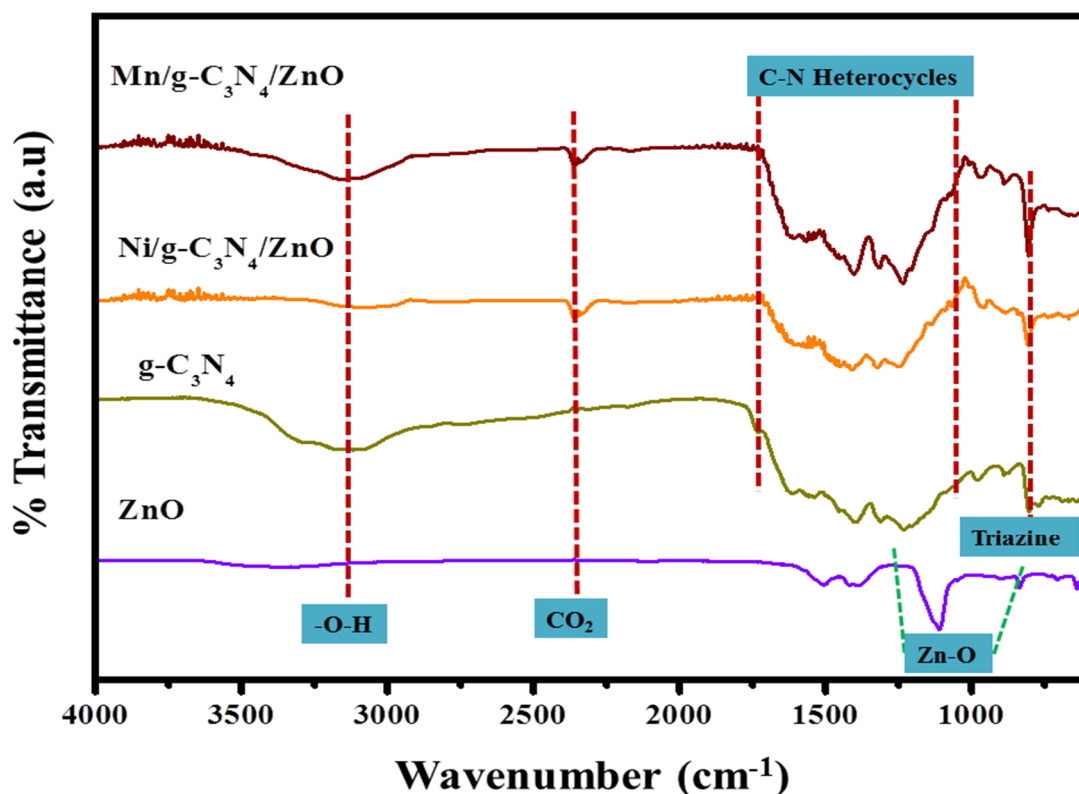


Figure 2. FTIR spectra of ZnO, $\text{g-C}_3\text{N}_4$, and (Ni/Mn)/ $\text{g-C}_3\text{N}_4$ /ZnO NCs.

3.2. XRD Analysis

X-ray diffractograms were used to characterize the phase and purity of the synthesized samples, as exhibited in Figure 3a,b. The XRD pattern of zinc oxide showed peaks (2θ values) with conforming crystal planes at 31.82° (100), 34.73° (002), 36.34° (101), 47.61° (102), 56.48° (110), 62.79° (103), 68.29° (112), and 69.41° (201), correspondingly, and these planes are recognized as the hexagonal wurtzite structure of ZnO (JCPDS # 043-0002) [46–49]. The $\text{g-C}_3\text{N}_4$ XRD pattern contained two distinct peaks at 13.02° and 27.3° , which correspond to the (100) and (002) facets of the crystals and confirmed its nanosheet morphology (JCPDS # 00-087-1526) [50,51]. The principal peaks ((100), (002), and (101)) in the XRD patterns of the Ni/GZ and Mn/GZ composites showed a minor decrease in intensity, supporting the successful incorporation of Ni/Mn metal ions into ZnO and its heterostructure development with $\text{g-C}_3\text{N}_4$ (Figure 3b) [52,53]. The successful synthesis of Ni/GZ and Mn/GZ composites is supported by the existence of characteristic $\text{g-C}_3\text{N}_4$ and ZnO diffraction peaks in the XRD patterns [17].

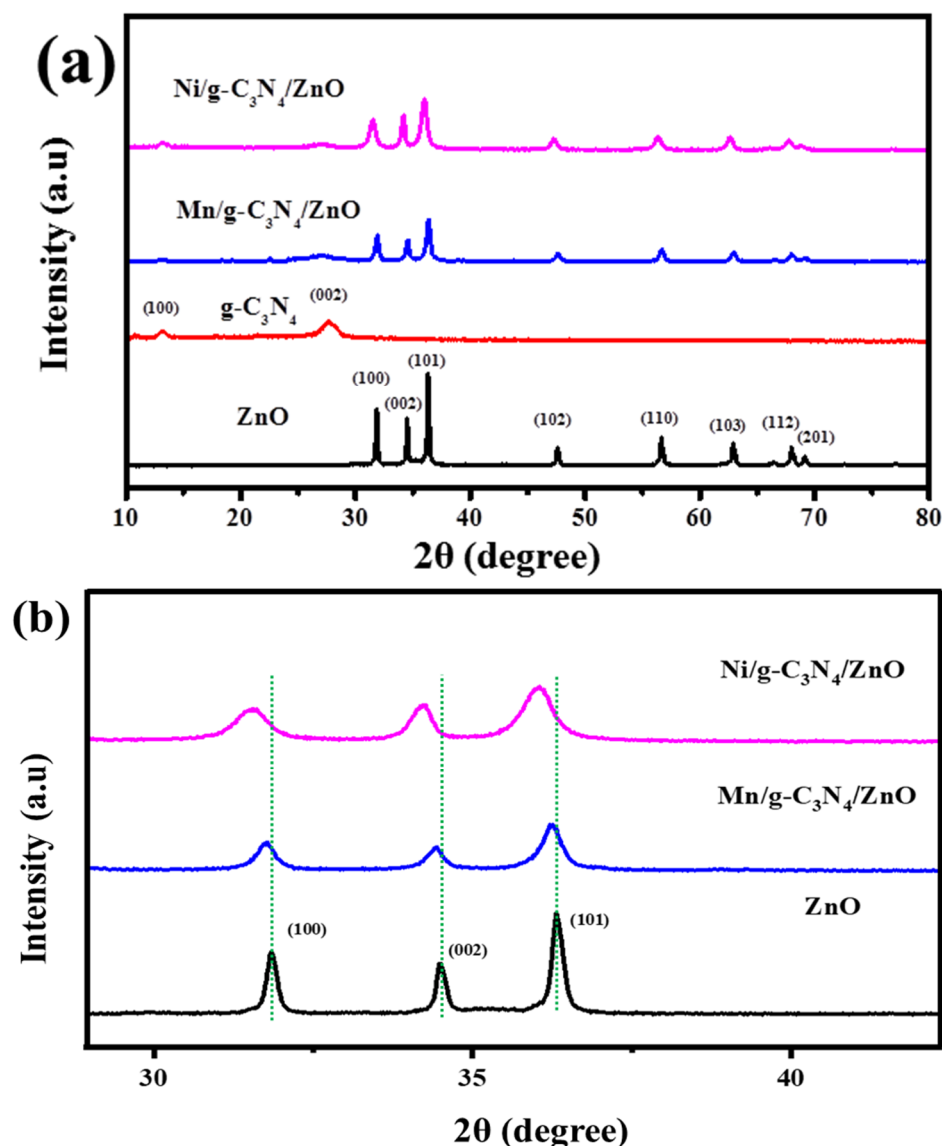


Figure 3. XRD patterns of ZnO, g-C₃N₄, and (Ni/Mn)/g-C₃N₄/ZnO NCs (a) Magnified XRD patterns of ZnO and (Ni/Mn)/g-C₃N₄/ZnO NCs (b).

3.3. Compositional and Morphological Study

To check the morphology and structural composition of the generated photocatalysts, TEM and SEM micrographs were acquired. The sphere-shaped morphology of ZnO NPs with 10–15 nm diameter is exhibited in Figure 4a. A lamellar sheet-like structure was observed for pure g-C₃N₄ in the TEM image (Figure 4b). The (Ni/Mn)-ZnO NPs were consistently integrated with thin sheets of g-C₃N₄, as exhibited in the TEM images of Mn/GZ (Figure 4c) and Ni/GZ (Figure 4d) NCs. The photocatalytic efficiency of the Ni/GZ and Mn/GZ NCs is improved by the correct integration of NPs into g-C₃N₄ layers, which aids quicker separation of e⁻/h⁺ pairs. The samples' exterior architecture was characterized by SEM, and the subsequent findings are shown in Figure 5a–d. The SEM image of ZnO NPs shows sphere-shaped particles (Figure 5a). Figure 5b shows the free g-C₃N₄ in the form of stacked thin sheets. The sheets are built up in piles to produce a bulk of nanosheets. The dispersal of spheroidal and rod-shaped particles on the g-C₃N₄ NSs was revealed in the scanning electron micrograph (SEM) picture of Ni/GZ NCs (Figure 5c), while the Mn/GZ NCs exhibited the fluffier sheet morphology, as shown in Figure 5d. It is widely accepted that this kind of composite shape considerably improves

the active sites and surface area, and, correspondingly, the catalytic proficiency of the heterojunction composites.

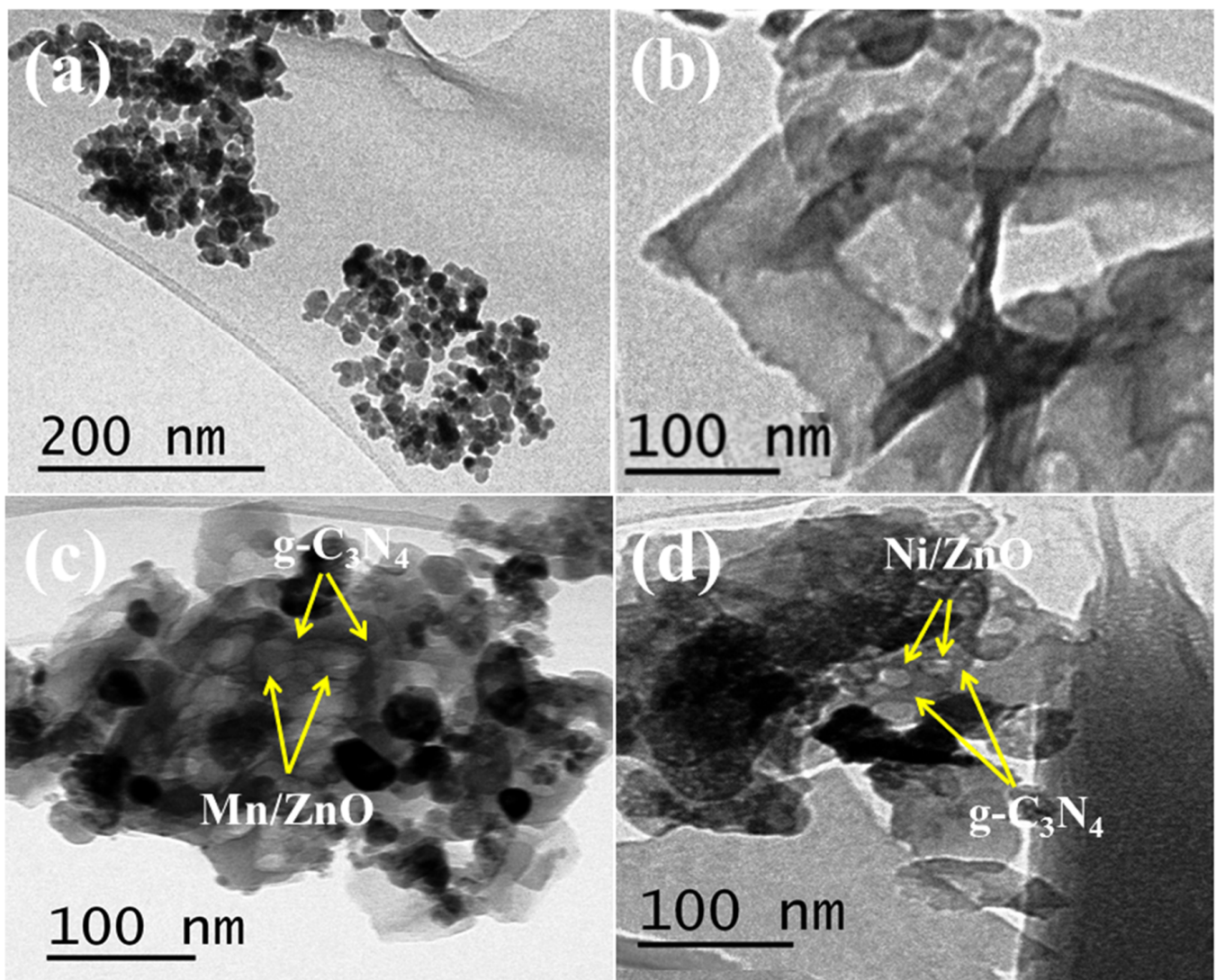


Figure 4. Morphological analysis of ZnO (a), g-C₃N₄ (b), Ni/g-C₃N₄/ZnO (c), and Mn/g-C₃N₄/ZnO (d) by TEM.

An EDX study was performed to determine the chemical and elemental makeup of the produced composites. The Zn and O peaks were seen in the ZnO EDX spectra, confirming the purity of NPs (Figure 6a). Only peaks for the elements carbon and nitrogen were seen in the EDX spectrum of g-C₃N₄ (Figure 6b). The EDX spectra of Ni/GZ (Figure 6c) and Mn/GZ (Figure 6d) NCs showed elemental peaks for carbon, nitrogen, zinc, and oxygen, in addition to peaks for nickel and manganese, respectively. The elemental data of each fabricated sample has been given by Tables S3–S6.

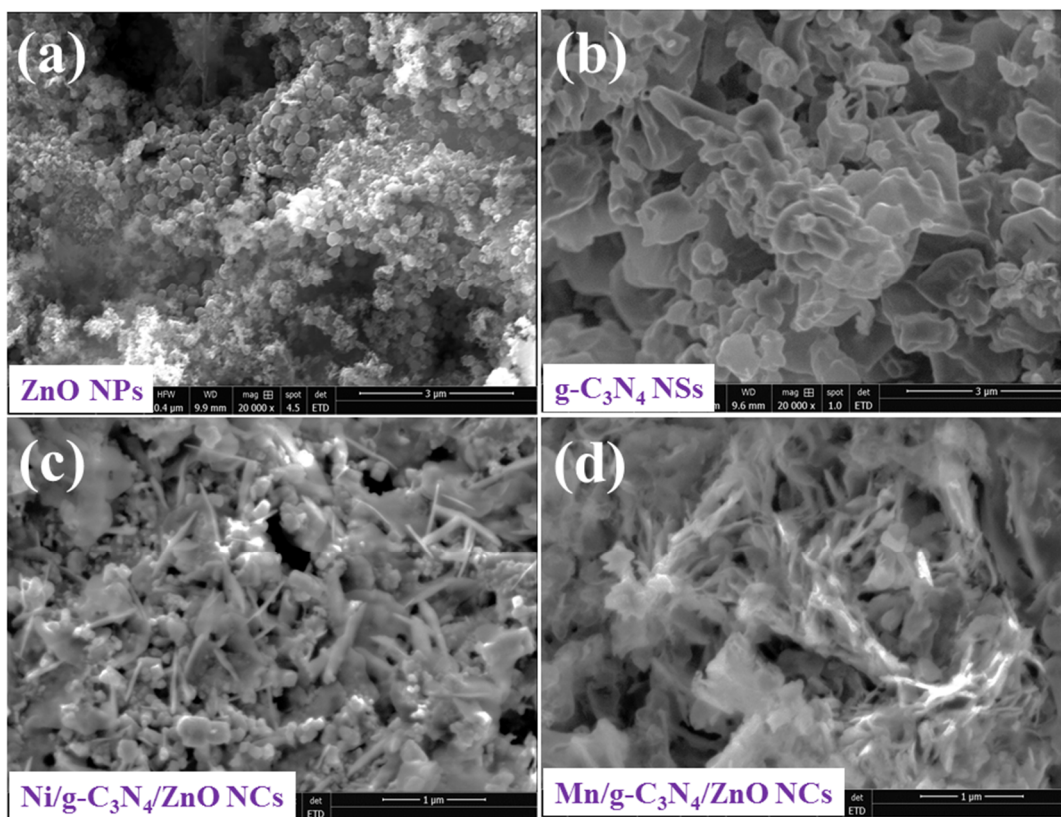


Figure 5. Morphological analysis of ZnO (a), g-C₃N₄ (b), Ni/g-C₃N₄/ZnO (c), and Mn/g-C₃N₄/ZnO (d) by SEM.

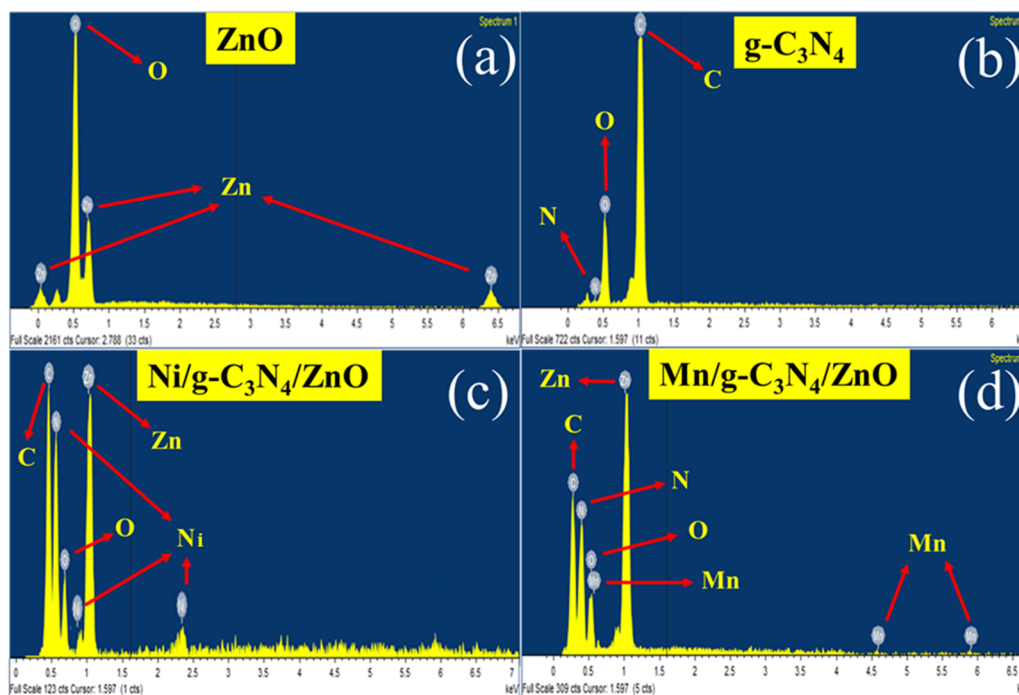


Figure 6. EDX analysis of ZnO (a), g-C₃N₄ (b), g-C₃N₄/ZnO (c), Ni/g-C₃N₄/ZnO (c), and Mn/g-C₃N₄/ZnO (d).

3.4. Optical Properties

UV-vis DRS experiments were employed to investigate the optical characteristics of the synthesized samples, as shown in Figure 7a. The corresponding E_g values of the synthesized samples were assessed by plotting the Kubelka-Munk function, as shown in Figure 7b [54]. The ZnO sample's reflectance band edge was about 375 nm, and it exhibited the greatest band gap value of 3.1 eV. In contrast, Mn/GZ NC had the smallest band gap energy of 1.9 eV. When g-C₃N₄ was incorporated into ZnO, the UV-vis reflectance decreased (or the absorption increased) throughout the entire wavelength range. These results are in accord with earlier results [55]. The band edge of GZ photocatalysts was somewhat expanded to a longer wavelength after adding g-C₃N₄. The same trend was also observed for Mn/GZ and Ni/GZ samples. Further, the integration of Ni/Mn ions into ZnO along with the addition of g-C₃N₄ broadened the light absorption of Mn/GZ and Ni/GZ photocatalysts into the visible region, as compared to that of pure ZnO [56]. The estimated band gap energies for GZ and Ni/GZ NC were 2.8 and 2.6 eV, respectively. These results indicate that the rate of e⁻/h⁺ pair recombination is reduced in Mn/GZ and Ni/GZ NCs.

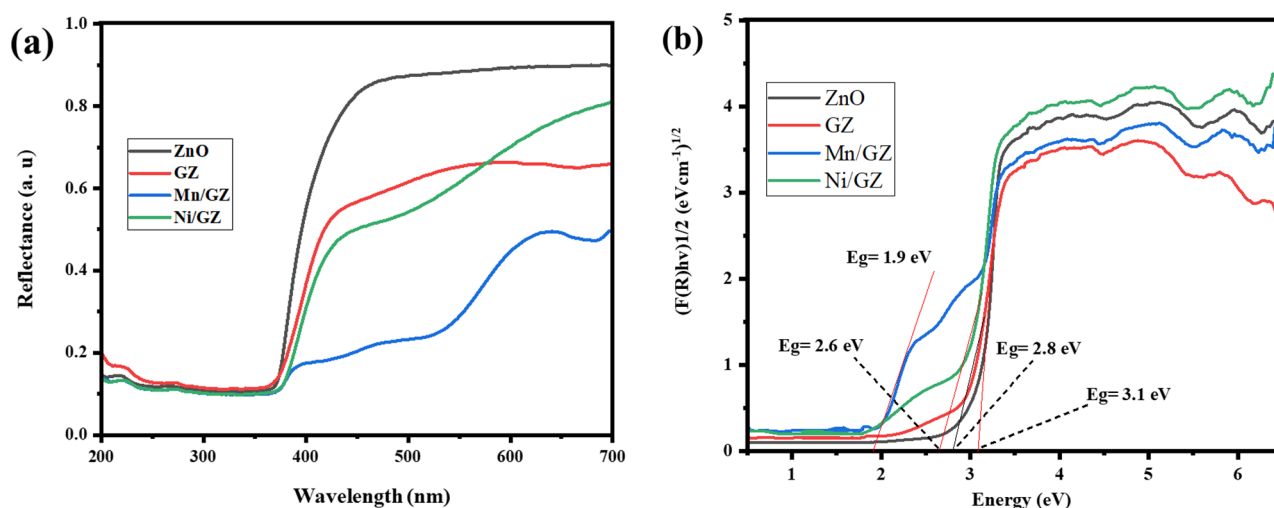


Figure 7. UV-vis DRS spectra (a) and band gap energy of ZnO, GZ, Mn/GZ, and Ni/GZ NCs (b).

3.5. Photocatalytic Study

The photocatalytic efficiency of the produced materials was observed under sunlight in two phases. In the first phase, the photocatalytic activity of the fabricated set of (Mn/Ni)/(20, 30, 40, 50, 60, 70, & 80) GZ NCs was investigated using EBT and MO solutions in sunlight (Figure 8a–d). The rates of dye decoloration were monitored using a UV-Vis spectrophotometer. To achieve adsorption-desorption equilibrium, each dye-composite solution was maintained in the dark for one hour before being exposed to the sun and realize the created materials' adsorption capacities. The Mn/GZ NCs in the adsorption experiment absorbed various amounts of EBT (Figure 8a) and MO dye (Figure 8b). The maximum dye adsorption (20% of EBT and 19% of MO) was observed for the Mn/50 GZ NCs as compared to other Mn/GZ NCs in the synthesized series. Likewise, in the adsorption experiment, the Ni/60 GZ NC revealed the best adsorption as compared to other Ni/GZ composites in the produced series (23% of EBT and 24% of MO).

The photocatalytic decoloration efficiency levels of Mn/g-C₃N₄/ZnO NCs against EBT and MO dyes are given by Figure 8a,b, respectively. The photocatalytic activity of Mn/GZ NCs increased with increasing concentration of g-C₃N₄ up to 50 wt.%. Thus, 50 wt.% g-C₃N₄ is the optimal concentration, and increasing the g-C₃N₄ concentration beyond this (<50 wt.%) causes a reduction in the photocatalytic efficiency of Mn/GZ NCs (Figure 8a,b). Under the impact of sunlight, the Mn/50GZ NC totally decolorized MO and EBT in 70 and 50 min, correspondingly. Likewise, Ni/60GZ NC showed the best photocatalytic efficiency against EBT and MO dyes as compared to other Ni/GZ NCs

(Figure 8c,d). The observed optimal concentration of $g\text{-C}_3\text{N}_4$ for Ni/GZ NCs was 60 wt.%. The Ni/60GZ NC completely decolorized EBT and MO in 60 and 90 min, respectively.

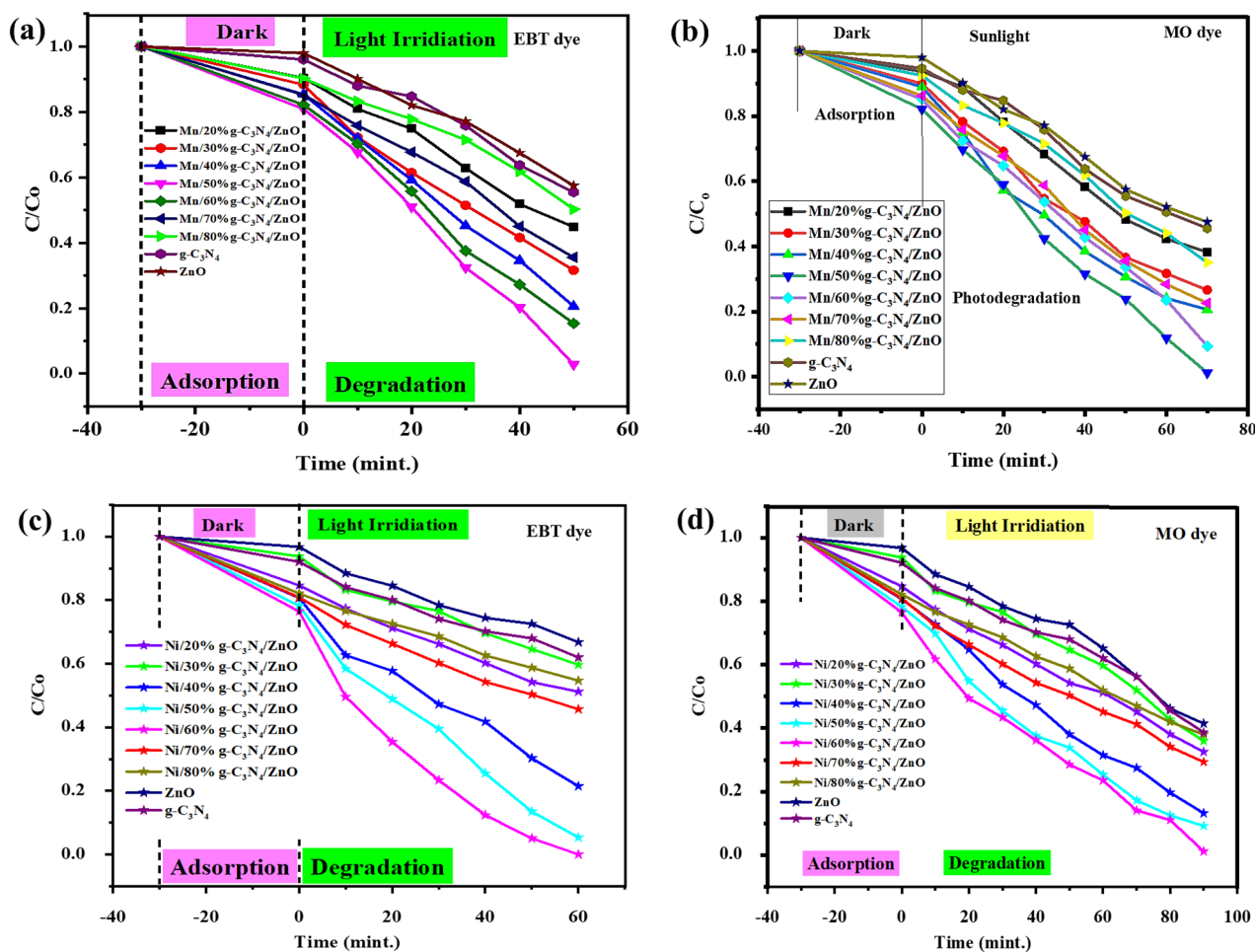


Figure 8. Photocatalytic decoloration rates of EBT (a) and MO dye (b) by Mn/50GZ NC, and decoloration rates of EBT (c) and MO dye (d) by Ni/60GZ NC.

There is a possibility that the greater charge separation is responsible for the better photocatalytic efficiency exhibited by the Ni/60GZ and Mn/50GZ NCs [57–59]. The Ni/60GZ and Mn/50GZ NCs would exhibit rapid charge transfer and higher absorption of visible radiation as a result of $g\text{-C}_3\text{N}_4$ coupling in ZnO, as well as doping with Mn and Ni. Intrinsically, for Ni/60GZ and Mn/50GZ NCs, the observed optimal weight proportions of $g\text{-C}_3\text{N}_4$ were 60% and 50%, respectively. A decreasing trend in photocatalytic proficiency was observed for NCs when the $g\text{-C}_3\text{N}_4$ concentration increased beyond the optimal limits. This might be because, if we increase the $g\text{-C}_3\text{N}_4$ contents, lengthier transport paths are generated for photoinduced charges, and extra charge recombination centers are created in the NCs [57–59]. A preliminary inquiry is needed to analyze this rationalization further.

In the second phase, the comparative photocatalytic efficiency of Mn/50GZ and Ni/60GZ NCs was observed against EBT and MO dyes. From Figure 9a–d, it is evident that Mn/50GZ NC had better photocatalytic efficiency than Ni/60GZ NCs against both dyes. According to recent research, the optical, electrical, and catalytic characteristics of $g\text{-C}_3\text{N}_4$ and ZnO are significantly improved by the addition of Mn and Ni. So, this could be a reason for the highest photocatalytic efficiency of the Mn/50GZ and Ni/60GZ NCs compared to $g\text{-C}_3\text{N}_4$ and ZnO. Additionally, Mn ions have a greater effect on the optical, electrical, and photocatalytic capabilities of $g\text{-C}_3\text{N}_4$ and ZnO than do Ni and other metal ions [60]. This could be the cause for the Mn/50GZ NC's superior photocatalytic activities when compared to Ni/60GZ NC and other synthesized composites.

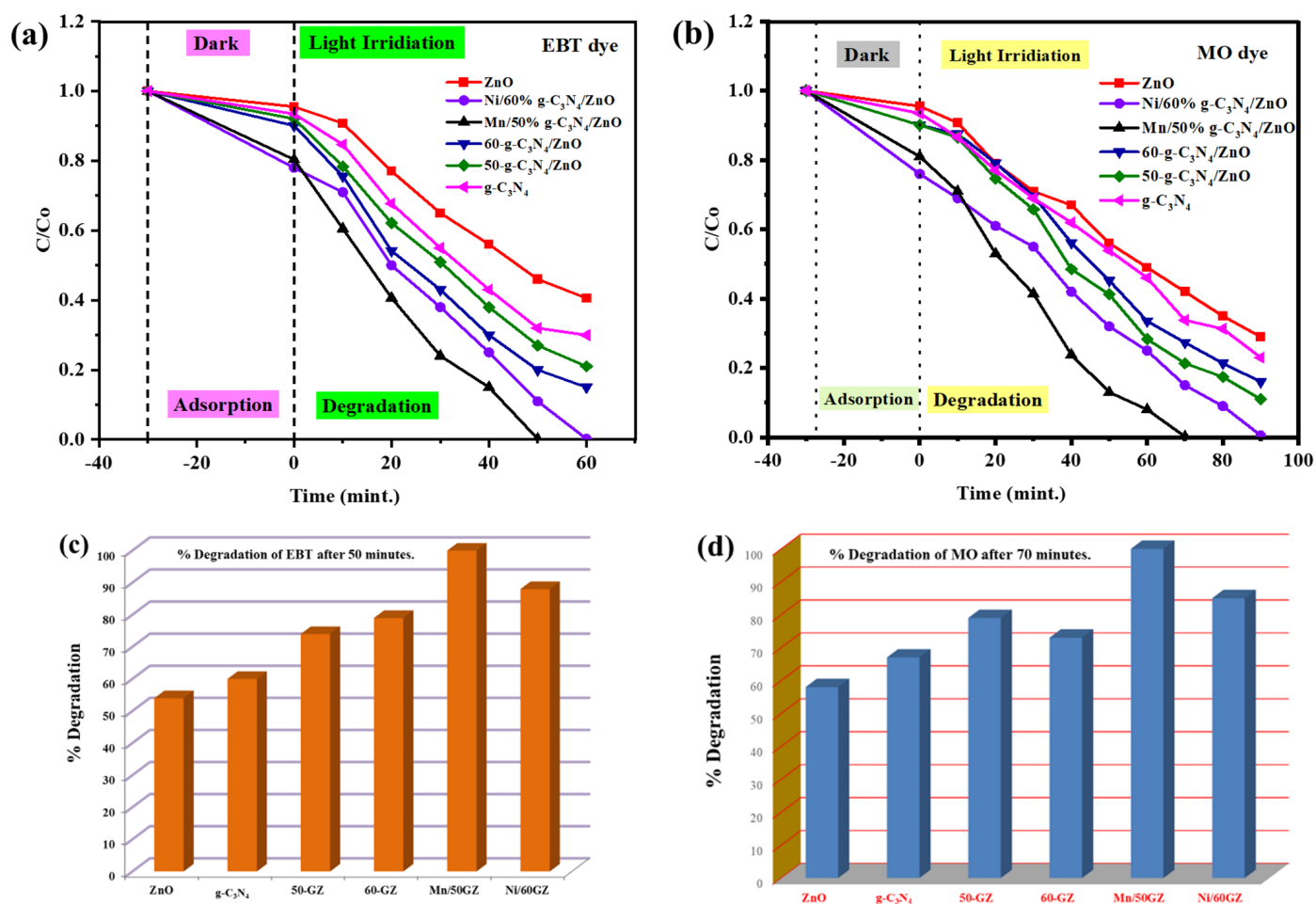


Figure 9. Photocatalytic dye decoloration rates of EBT (a) and MO (b) and bar graphs of the percentage of decoloration of EBT (c) and MO (d) by Ni/60GZ, Mn/50GZ, 50-GZ, 60-GZ, and g-C₃N₄.

The kinetics of EBT dye decolorization are explained by the Langmuir-Hinshelwood model for ZnO, g-C₃N₄, Ni/60GZ, Mn/50GZ, 60% g-C₃N₄/ZnO, and 50% g-C₃N₄/ZnO NCs, as shown in Figure 10a,b [61]. Figure 10a makes it clear that the EBT dye decoloration by the manufactured samples when exposed to sunlight fits to pseudo-first-order dynamics. The determined values of each NC's decolorization rate constant (k) are displayed as a bar graph in Figure 10b. The highest and lowest " k " values were found in Mn/50GZ (0.027 min^{-1}) and ZnO (0.008 min^{-1}). The Mn/50GZ NCs totally decolorated the EBT in 50 min, and their " k " value is 3.3 and 2.58 times higher than those of ZnO (0.008 min^{-1}) and g-C₃N₄ (0.0105 min^{-1}), which both decolorated the EBT in less time. The maximum " k " value for Mn/50GZ supports the maximal synergic activity of g-C₃N₄, Mn, and ZnO in Mn/50GZ NC, which increased the composite's active sites and photocatalytic efficiency against EBT dye. Similarly, the observed kinetics of MO dye decoloration by ZnO, g-C₃N₄, Ni/60GZ, Mn/50GZ, 60% g-C₃N₄/ZnO, and 50% g-C₃N₄/ZnO NCs are given in Figure 10c,d. The photocatalytic efficiency of Mn/50GZ and Ni/60GZ NCs was significantly higher than those in various prior reported research, as given in Table 1 [62–67]. The most effective photocatalyst was utilized in the recycling study, which was Mn/50GZ NC.

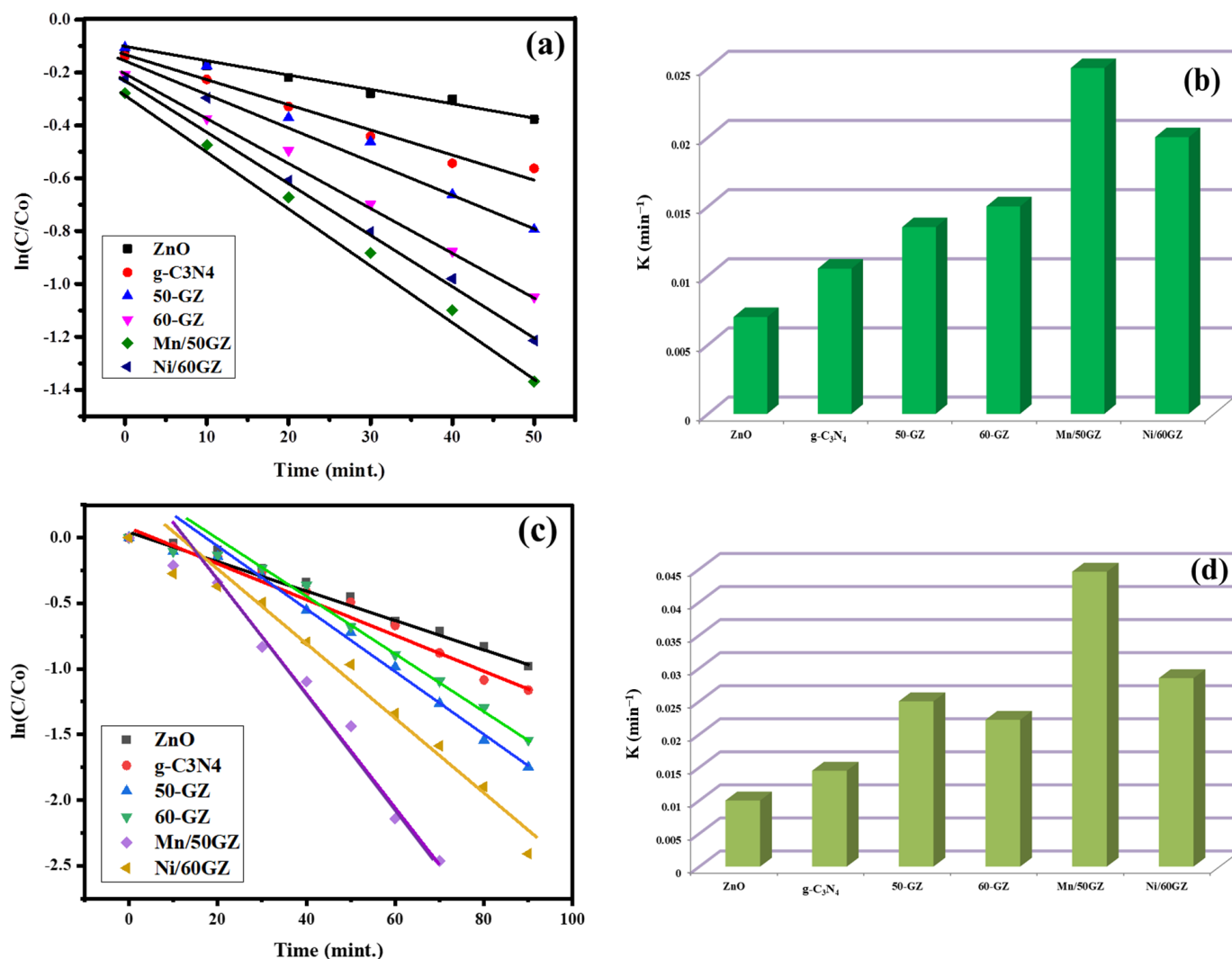


Figure 10. EBT decoloration kinetic characteristics (a) and k (min^{-1}) values (b) and MO decoloration kinetic characteristics (c) and k (min^{-1}) values (d) by Ni/60GZ, Mn/50GZ, 50-GZ, 60-GZ, and g-C₃N₄.

Table 1. Comparison of decoloration capabilities of Mn/50GZ with some earlier works.

Sr. No	Photocatalyst	Contaminant	Light Source	Dye (mg/L)	Catalyst (mg/L)	Radiation Time (min.)	Decoloration%	Ref.
1	Mn-ZnO/CSAC	BG	Sunlight	30	200	175	96	[62]
2	ZnO/Fe ₂ O ₄ /Pt	Ciprofloxacin	Xe lamp	10	150	75	100	[63]
3	Mn-ZnO/RGO	RhB	Visible	20	20	140	99	[58]
4	ZnO/ZnFe ₂ O ₄	MB	Visible	10	50	100	98	[64]
5	Pt-BiFeO ₃	MG	Visible	10	100	240	96	[65]
6	ZnO/Fe ₃ O ₄ /g-C ₃ N ₄	MO	Visible	30	10	150	97.87	[66]
7	Mn-ZnO/CNT	MG	Visible	50	100	150	>95	[57]
8	ZnFe ₂ O ₄ @ZnO	MO	Visible	56	660	240	99	[67]
9	Mn/50% g-C ₃ N ₄ /ZnO	EBT	Sunlight	10	200	50	100	Present work

3.6. Photoluminescence Spectra

An important method frequently used to assess the photo-excited (e^-/h^+ pairs) charge separation capability in photocatalytic systems is photoluminescence (PL) spectroscopy [68]. The PL emission spectra of the produced photocatalysts at 365 nm excitation wavelength are shown in Figure S1. The strong emission peak for $g\text{-C}_3\text{N}_4$ can be seen at about 440 nm, which indicates a high rate of recombination for the photo-excited $e-h$ pair of graphitic carbon nitride. When compared to ZnO, Mn/50GZ and Ni/60GZ exhibit a significant decrease in PL intensity. This decrease may be attributed to zinc defects, surface oxygen vacancies, and the growth of Mn/50GZ and Ni/60GZ heterostructures [69]. Mn/50GZ exhibited the smallest PL peak, demonstrating that the strong junction between the Mn, ZnO, and $g\text{-C}_3\text{N}_4$ sheets strongly inhibits $e-h$ pair recombination as compared to the Ni/60GZ heterostructure. This finding demonstrates that the photo-excited electrons used in the generation of reactive oxygen species (ROS) are productively conducted by the Mn/50GZ and Ni/60GZ nanocomposites. As a result, the rate of charge recombination is decreased, and Mn/50GZ and Ni/60GZ NC photocatalytic competence is increased.

3.7. Recyclability and Constancy of the Mn/50GZ Composite

A photocatalyst must sustain its stability and endurance under repeated photocatalytic activities in order to be useful in practical applications. Five consecutive photocatalytic recycling experiments were performed to monitor the stability of the Mn/50GZ NC. In the recyclability test, the Mn/50GZ NC kept up its rate of dye degradation. The composite's dye decoloration efficiency did not decrease significantly even after the fifth recycle, as shown in Figure 11a. Interestingly, following the fifth cycle, there were no discernible variations in the XRD profile of the Mn/50GZ NC (Figure 11b). Possible explanations for the small reduction in catalytic efficiency of the nanocomposite involve partial blockage of active sites. The Mn/50GZ NC might thus function as a reliable, reusable, and efficient photocatalytic material.

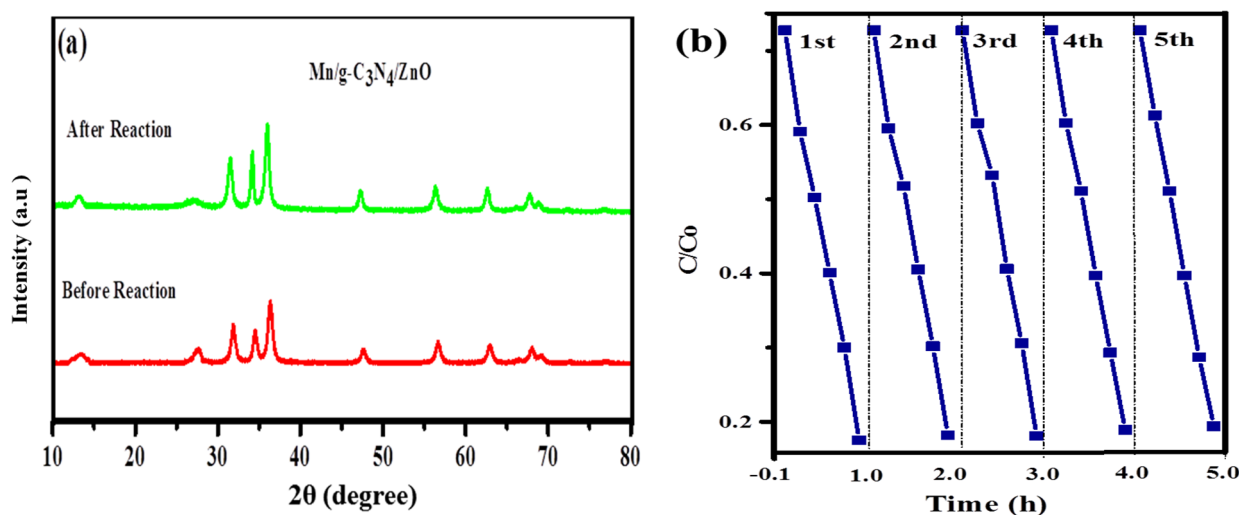


Figure 11. XRD analysis of Mn/50GZ NCs (a) and the recyclability test (b) after the fifth cycle.

It is crucial to identify the fundamental ROS photoinduced by the Mn/GZ and Ni/GZ NCs responsible for the photocatalytic decomposition of dyes. In order to investigate the potential mechanism of photocatalytic dye decoloration, three chemical traps were employed to capture the ROS generated during the dye decoloration reaction. The influence of the trapping compounds on the dye decoloration reaction is shown in Figure 12a,b. The results show that $\bullet\text{OH}$ and $\bullet\text{O}_2^-$ are the principal reactive species involved in the photocatalytic dye degradation, with 91% and 60% inhibition, respectively. On the other hand, h^+ , accounting for 14% of the inhibition, is the lesser oxidative species engaging in dye photodegradation.

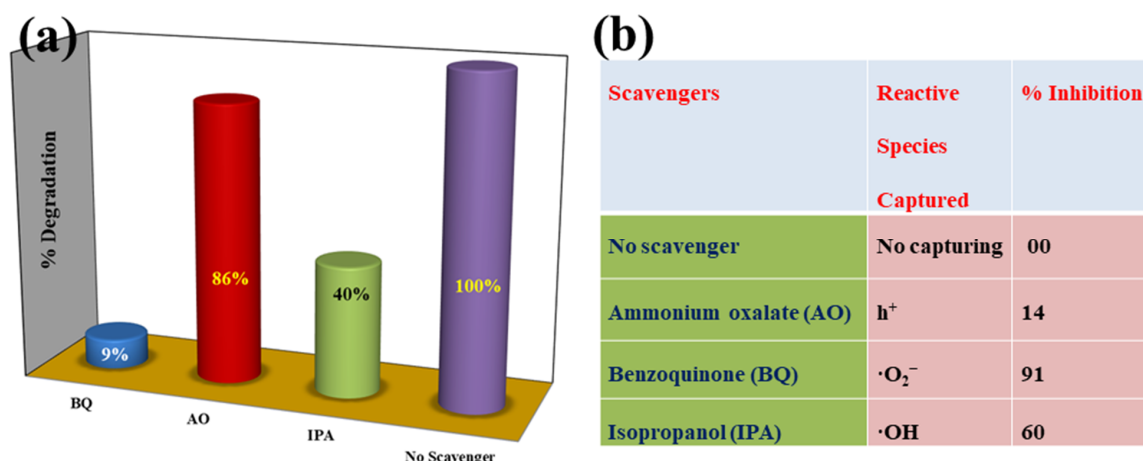


Figure 12. Scavenger effects (a) and the capture of reactive species with percentage inhibition (b).

3.8. Mechanism

The enhanced decoloration of EBT/MO dyes by Ni/GZ and Mn/GZ NCs may be accredited to the production of e^-/h^+ pairs in the produced photocatalysts, as shown via schematic sketch (Figure 13). When sunlight irradiates the NCs, both ZnO and $g-C_3N_4$ are excited, and $e/h+$ couples are formed on their respective conduction bands (CB) and valence bands (VB) [18]. ZnO and $g-C_3N_4$ valence bond electrons are promoted to their conduction bands. The excited electrons from the CB of $g-C_3N_4$ (-1.12 eV) are transported to the CB of ZnO (-0.5 eV). On the basis of the CB/VB edge potentials, Photo-induced electrons may easily migrate from the $g-C_3N_4$ conduction band (CB) to the CB of ZnO. Simultaneously, the h^+ in the VB of ZnO might shift to $g-C_3N_4$, because ZnO has higher VB potential than $g-C_3N_4$ [70]. To enhance the electron transportation and reduce $e/h+$ pair recombination, the Mn/Ni metal ions in the Mn/GZ and Ni/GZ NCs not only function as a facilitator at the $g-C_3N_4$ and ZnO interface but also decrease the E_g value of ZnO [62]. The produced e and $h+$ react with the water and oxygen adsorbed on the photocatalyst surface to form radicals ($\cdot OH$ and $\cdot O_2^-$) [71]. These radicals are used to decolorize dye molecules by converting them into low-molecular-weight intermediates, which are then oxidized into H_2O , CO_2 , and inorganic ions.

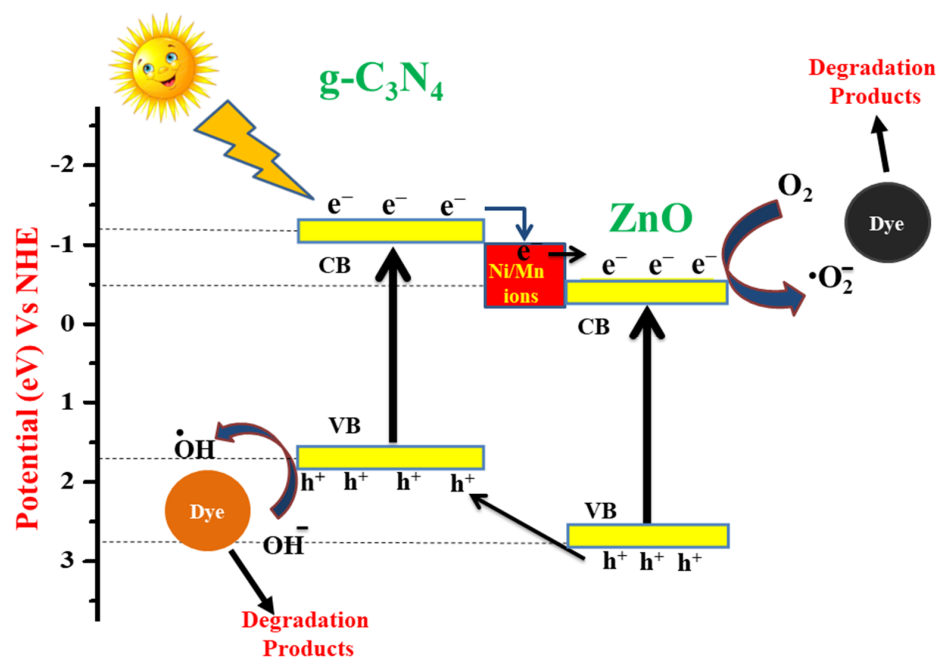


Figure 13. Mechanism of MO/EBT dye photocatalytic decoloration using Mn/GZ and Ni/GZ NCs as photocatalysts.

4. Conclusions

In this study, extremely effective (Mn/Ni)/g-C₃N₄/ZnO (Mn/GZ and Ni/GZ) photocatalysts were made via the co-precipitation method. The assembly and purity of the samples were studied using the XRD, TEM, SEM, EDX, and FTIR methods. Photocatalytic dye decoloration testing of the synthesized (Mn/Ni)/(20, 30, 40, 50, 60, 70, and 80) GZ samples was carried out against MO and EBT, and it was observed that the Mn/50GZ NCs had a very high decolorizing efficiency under sunlight. The Mn/50GZ NC completely decolorized EBT and MO in 50 and 70 min, respectively, while Ni/60GZ NC decolorized the same dyes in 60 and 90 min, respectively. Further, Mn/GZ and Ni/GZ NCs exhibited pseudo-first-order kinetics during the dye-reduction reaction. The number of active sites, surface defects, and reduction in e⁻/h⁺ pairs in nanocomposites were improved by the successful integration of metal ions, ZnO, on the fragile sheets of g-C₃N₄, as exhibited by TEM images and PL study. In general, the findings of this work contribute to a better understanding of the processes involved in synthesizing photocatalysts and their uses for the decoloration of organic pollutants from wastewater.

Supplementary Materials: The following supporting information can be downloaded at: <https://www.mdpi.com/article/10.3390/catal12111388/s1>, Figure S1: Photoluminescence spectra of ZnO, Ni/60GZ, Mn/50GZ, and g-C₃N₄ samples; Table S1: Composition of the synthesized Ni/g-C₃N₄/ZnO composites; Table S2: Composition of the synthesized Mn/g-C₃N₄/ZnO composites; Table S3: Elemental data of ZnO nanoparticles; Table S4: Elemental data of g-C₃N₄ nanosheets; Table S5: Elemental data of Mn/g-C₃N₄/ZnO nanocomposites; Table S6: Elemental data of Ni/g-C₃N₄/ZnO nanocomposites.

Author Contributions: Formal analysis, M.S. and O.M.; methodology, M.J. and S.K.A.; resources, M.M.F. and M.S.K.; software, M.Y.A.; supervision, S.S. and M.J.; validation, M.H.A.N.; visualization, I.S.S. and D.A.H.; writing – original draft, M.A.Q.; writing—review & editing, S.S. All authors have read and agreed to the published version of the manuscript.

Funding: This research work was funded by the Deanship of Scientific Research at Majmaah University, under Project Number R-2022-335, Al Majmaah, Saudi Arabia.

Data Availability Statement: Not applicable.

Acknowledgments: The authors would like to thank the Deanship of Scientific Research at Majmaah University for supporting this work under Project Number R-2022-335.

Conflicts of Interest: The authors disclose no possible conflict of interest.

References

1. Finke, E.-J.; Beyer, W.; Loderstädt, U.; Frickmann, H. The risk of contracting anthrax from spore-contaminated soil—A military medical perspective. *Eur. J. Microbiol. Immunol.* **2020**, *10*, 29–63. [[CrossRef](#)] [[PubMed](#)]
2. Zou, L.; Wang, H.; Jiang, X.; Yuan, G.; Wang, X. Enhanced photocatalytic efficiency in degrading organic dyes by coupling CdS nanowires with ZnFe₂O₄ nanoparticles. *Sol. Energy* **2020**, *195*, 271–277. [[CrossRef](#)]
3. Basaleh, A. Construction of mesoporous ZnFe₂O₄-g-C₃N₄ nanocomposites for enhanced photocatalytic degradation of acridine orange dye under visible light illumination adopting soft-and hard-template-assisted routines. *J. Mater. Res. Technol.* **2021**, *11*, 1260–1271. [[CrossRef](#)]
4. Dhasmana, A.; Uniyal, S.; Kumar, V.; Gupta, S.; Kesari, K.K.; Haque, S.; Lohani, M.; Pandey, J. Scope of nanoparticles in environmental toxicant remediation. In *Environmental Biotechnology: For Sustainable Future*; Springer: Singapore, 2019; pp. 31–44.
5. Sharma, S.; Dutta, V.; Raizada, P.; Hosseini-Bandegharai, A.; Thakur, V.; Nguyen, V.-H.; VanLe, Q.; Singh, P. An overview of heterojunctioned ZnFe₂O₄ photocatalyst for enhanced oxidative water purification. *J. Environ. Chem. Eng.* **2021**, *9*, 105812.
6. Alshorifi, F.T.; Alswat, A.A.; Mannaa, M.A.; Alotaibi, M.T.; El-Bahy, S.M.; Salama, R.S. Facile and Green Synthesis of Silver Quantum Dots Immobilized onto a Polymeric CTS-PEO Blend for the Photocatalytic Degradation of p-Nitrophenol. *ACS Omega* **2021**, *6*, 30432–30441. [[CrossRef](#)]
7. Pirhashemi, M.; Habibi-Yangjeh, A.; Pouran, S.R. Review on the criteria anticipated for the fabrication of highly efficient ZnO-based visible-light-driven photocatalysts. *J. Ind. Eng. Chem.* **2018**, *62*, 1–25. [[CrossRef](#)]
8. Jilani, A.; Ansari, M.O.; Ur Rehman, G.; Shakoor, M.B.; Hussain, S.Z.; Othman, M.H.D.; Ahmad, S.R.; Dustgeer, M.R.; Alshahrie, A. Phenol removal and hydrogen production from water: Silver nanoparticles decorated on polyaniline wrapped zinc oxide nanorods. *J. Ind. Eng. Chem.* **2022**, *109*, 347–358. [[CrossRef](#)]

9. Shekofteh-Gohari, M.; Habibi-Yangjeh, A.; Abitorabi, M.; Rouhi, A. Magnetically separable nanocomposites based on ZnO and their applications in photocatalytic processes: A review. *Crit. Rev. Environ. Sci. Technol.* **2018**, *48*, 806–857. [[CrossRef](#)]
10. Jin, Y.; Long, J.; Ma, X.; Zhou, T.; Zhang, Z.; Lin, H.; Long, J.; Wang, X. Synthesis of caged iodine-modified ZnO nanomaterials and study on their visible light photocatalytic antibacterial properties. *Appl. Catal. B Environ.* **2019**, *256*, 117873. [[CrossRef](#)]
11. Kuang, M.; Zhang, J.; Wang, W.; Chen, J.; Liu, R.; Xie, S.; Wang, J.; Ji, Z. Synthesis of octahedral-like ZnO/ZnFe₂O₄ heterojunction photocatalysts with superior photocatalytic activity. *Solid State Sci.* **2019**, *96*, 105901. [[CrossRef](#)]
12. Umar, K.; Adnan, R. Biomass Mediated Green Synthesis of ZnO/TiO₂ Nanocomposite and Enhanced Photocatalytic Activity for the Decolorization of Rhodamine B under Visible Light. In *Key Engineering Materials*; Trans Tech Publications Ltd.: Zurich, Switzerland, 2022; pp. 36–42.
13. Hong, J.; Xia, X.; Wang, Y.; Xu, R. Mesoporous carbon nitride with in situ sulfur doping for enhanced photocatalytic hydrogen evolution from water under visible light. *J. Mater. Chem.* **2012**, *22*, 15006–15012. [[CrossRef](#)]
14. Djerdj, I.; Jagličić, Z.; Arčon, D.; Niederberger, M. Co-doped ZnO nanoparticles: Minireview. *Nanoscale* **2010**, *2*, 1096–1104. [[CrossRef](#)] [[PubMed](#)]
15. Chauhan, N.; Singh, V.; Kumar, S.; Dhiman, R. Influence of nickel, silver, and sulphur doping on the photocatalytic efficiency of mesoporous ZnO nanoparticles. *Arab. J. Sci. Eng.* **2020**, *45*, 249–259. [[CrossRef](#)]
16. Ahmad, I. Comparative study of metal (Al, Mg, Ni, Cu and Ag) doped ZnO/g-C₃N₄ composites: Efficient photocatalysts for the degradation of organic pollutants. *Sep. Purif. Technol.* **2020**, *251*, 117372. [[CrossRef](#)]
17. Zhang, S.; Su, C.; Ren, H.; Li, M.; Zhu, L.; Ge, S.; Wang, M.; Zhang, Z.; Li, L.; Cao, X. In-situ fabrication of g-C₃N₄/ZnO nanocomposites for photocatalytic degradation of methylene blue: Synthesis procedure does matter. *Nanomaterials* **2019**, *9*, 215. [[CrossRef](#)]
18. Zhang, H.; Zhu, C.; Zhang, G.; Li, M.; Tang, Q.; Cao, J. Palladium modified ZnFe₂O₄/g-C₃N₄ nanocomposite as an efficiently magnetic recycling photocatalyst. *J. Solid State Chem.* **2020**, *288*, 121389. [[CrossRef](#)]
19. Chen, Z.; Zhang, S.; Liu, Y.; Alharbi, N.S.; Rabah, S.O.; Wang, S.; Wang, X. Synthesis and fabrication of g-C₃N₄-based materials and their application in elimination of pollutants. *Sci. Total Environ.* **2020**, *731*, 139054. [[CrossRef](#)]
20. Bai, X.; Wang, L.; Zong, R.; Zhu, Y. Photocatalytic activity enhanced via g-C₃N₄ nanoplates to nanorods. *J. Phys. Chem. C* **2013**, *117*, 9952–9961. [[CrossRef](#)]
21. Wang, X.; Chen, X.; Thomas, A.; Fu, X.; Antonietti, M. Metal-containing carbon nitride compounds: A new functional organic-metal hybrid material. *Adv. Mater.* **2009**, *21*, 1609–1612. [[CrossRef](#)]
22. Dong, F.; Sun, Y.; Wu, L.; Fu, M.; Wu, Z. Facile transformation of low cost thiourea into nitrogen-rich graphitic carbon nitride nanocatalyst with high visible light photocatalytic performance. *Catal. Sci. Technol.* **2012**, *2*, 1332–1335. [[CrossRef](#)]
23. Shen, B.; Hong, Z.; Chen, Y.; Lin, B.; Gao, B. Template-free synthesis of a novel porous g-C₃N₄ with 3D hierarchical structure for enhanced photocatalytic H₂ evolution. *Mater. Lett.* **2014**, *118*, 208–211. [[CrossRef](#)]
24. Chang, F.; Xie, Y.; Li, C.; Chen, J.; Luo, J.; Hu, X.; Shen, J. A facile modification of g-C₃N₄ with enhanced photocatalytic activity for degradation of methylene blue. *Appl. Surf. Sci.* **2013**, *280*, 967–974. [[CrossRef](#)]
25. Kuriki, R.; Sekizawa, K.; Ishitani, O.; Maeda, K. Visible-light-driven CO₂ reduction with carbon nitride: Enhancing the activity of ruthenium catalysts. *Angew. Chem. Int. Ed.* **2015**, *54*, 2406–2409. [[CrossRef](#)] [[PubMed](#)]
26. Mao, L.; Jin, H.; Wang, M.; Hu, Y.; Chen, S.; He, Q.; Chang, J.; Hong, C.; Zhou, Y.; Wang, D. Neurologic manifestations of hospitalized patients with coronavirus disease 2019 in Wuhan, China. *JAMA Neurol.* **2020**, *77*, 683–690. [[CrossRef](#)]
27. Guo, Y.; Sun, X.; Chen, Q.; Liu, Y.; Lou, X.; Zhang, L.; Zhang, X.; Li, Y.; Guan, J. Photocatalytic Applications of g-C₃N₄ Based on Bibliometric Analysis. *Catalysts* **2022**, *12*, 1017. [[CrossRef](#)]
28. Suzuki, V.Y.; Amorin, L.H.; Fabris, G.S.; Dey, S.; Sambrano, J.R.; Cohen, H.; Oron, D.; La Porta, F.A. Enhanced Photocatalytic and Photoluminescence Properties Resulting from Type-I Band Alignment in the Zn₂GeO₄/g-C₃N₄ Nanocomposites. *Catalysts* **2022**, *12*, 692. [[CrossRef](#)]
29. Machín, A.; Fontánez, K.; Duconge, J.; Cotto, M.C.; Petrescu, F.I.; Morant, C.; Márquez, F. Photocatalytic degradation of fluoroquinolone antibiotics in solution by Au@ZnO-rGO-gC₃N₄ composites. *Catalysts* **2022**, *12*, 166. [[CrossRef](#)]
30. Yaqoob, A.; Mohd Noor, N.H.B.; Umar, K.; Adnan, R.; Ibrahim, M.N.M.; Rashid, M. Graphene oxide-ZnO nanocomposite: An efficient visible light photocatalyst for degradation of rhodamine B. *Appl. Nanosci.* **2021**, *11*, 1291–1302. [[CrossRef](#)]
31. Li, L.; Sun, S.-Q.; Wang, Y.-X.; Wang, C.-Y. Facile synthesis of ZnO/g-C₃N₄ composites with honeycomb-like structure by H₂ bubble templates and their enhanced visible light photocatalytic performance. *J. Photochem. Photobiol. A Chem.* **2018**, *355*, 16–24. [[CrossRef](#)]
32. Wang, J.-C.; Cui, C.-X.; Li, Y.; Liu, L.; Zhang, Y.-P.; Shi, W. Porous Mn doped g-C₃N₄ photocatalysts for enhanced synergetic degradation under visible-light illumination. *J. Hazard. Mater.* **2017**, *339*, 43–53. [[CrossRef](#)]
33. Wang, M.; Guo, P.; Zhang, Y.; Lv, C.; Liu, T.; Chai, T.; Xie, Y.; Wang, Y.; Zhu, T. Synthesis of hollow lantern-like Eu (III)-doped g-C₃N₄ with enhanced visible light photocatalytic performance for organic degradation. *J. Hazard. Mater.* **2018**, *349*, 224–233. [[CrossRef](#)] [[PubMed](#)]
34. Tonda, S.; Kumar, S.; Kandula, S.; Shanker, V. Fe-doped and-mediated graphitic carbon nitride nanosheets for enhanced photocatalytic performance under natural sunlight. *J. Mater. Chem. A* **2014**, *2*, 6772–6780. [[CrossRef](#)]

35. Wu, L.; Liu, X.; Lv, G.; Zhu, R.; Tian, L.; Liu, M.; Li, Y.; Rao, W.; Liu, T.; Liao, L. Study on the adsorption properties of methyl orange by natural one-dimensional nano-mineral materials with different structures. *Sci. Rep.* **2021**, *11*, 10640. [[CrossRef](#)] [[PubMed](#)]
36. Boudouaia, N.; Bengharez, Z.; Jellali, S. Preparation and characterization of chitosan extracted from shrimp shells waste and chitosan film: Application for Eriochrome black T removal from aqueous solutions. *Appl. Water Sci.* **2019**, *9*, 91. [[CrossRef](#)]
37. Shi, L.; Liang, L.; Ma, J.; Wang, F.; Sun, J. Remarkably enhanced photocatalytic activity of ordered mesoporous carbon/g-C₃N₄ composite photocatalysts under visible light. *Dalton Trans.* **2014**, *43*, 7236–7244. [[CrossRef](#)]
38. Sher, M.; Shahid, S.; Javed, M. Synthesis of a novel ternary (g-C₃N₄ nanosheets loaded with Mo doped ZnO nanoparticles) nanocomposite for superior photocatalytic and antibacterial applications. *J. Photochem. Photobiol. B Biol.* **2021**, *219*, 112202. [[CrossRef](#)]
39. Slobodan, D.; Nada, T.; Zhiyu, P. Absorption spectroscopy of EBT model GAFCHROMIC™ film. *Med. Phys.* **2007**, *34*, 2207.
40. Jethave, G.; Fegade, U.; Attarde, S.; Ingle, S. Decontamination study of Eriochrome Black-T from waste water by using AlTiPbO nanoparticles (ATPO-NPs) for sustainable clean environment. *J. Water Environ. Nanotechnol.* **2019**, *4*, 263–274.
41. Jamshidi, E.; Manteghi, F. Methyl Orange Adsorption by Fe₂O₃@ Co-Al-Layered Double Hydroxide. *Multidiscip. Digit. Publ. Inst. Proc.* **2020**, *41*, 64.
42. Qamar, M.A.; Shahid, S.; Javed, M. Synthesis of dynamic g-C₃N₄/Fe@ ZnO nanocomposites for environmental remediation applications. *Ceram. Int.* **2020**, *46*, 22171–22180. [[CrossRef](#)]
43. Palanivel, B.; Maiyalagan, T.; Jayarman, V.; Ayyappan, C.; Alagiri, M. Rational design of ZnFe₂O₄/g-C₃N₄ nanocomposite for enhanced photo-Fenton reaction and supercapacitor performance. *Appl. Surf. Sci.* **2019**, *498*, 143807. [[CrossRef](#)]
44. Saeed, H.; Nadeem, N.; Zahid, M.; Yaseen, M.; Noreen, S.; Jilani, A.; Shahid, I. Mixed metal ferrite (Mn_{0.6}Zn_{0.4}Fe₂O₄) intercalated g-C₃N₄ nanocomposite: Efficient sunlight driven photocatalyst for methylene blue degradation. *Nanotechnology* **2021**, *32*, 505714. [[CrossRef](#)] [[PubMed](#)]
45. Xiao, Z.; Liming, W.; Yong, S.; Lihui, X.; Mingrui, X. Preparation and photocatalytic properties of magnetic g-C₃N₄/MnZnFe₂O₄ composite. *J. Phys. Conf. Ser.* **2021**, *1790*, 012075. [[CrossRef](#)]
46. Shanmugam, N.; Suthakaran, S.; Kannadasan, N.; Sathishkumar, K. Synthesis and characterization of Te doped ZnO nanosheets for photocatalytic application. *JO Heterocycl.* **2015**, *105*, 15–20. [[CrossRef](#)]
47. Ahmad, A.; Wei, Y.; Syed, F.; Tahir, K.; Rehman, A.U.; Khan, A.; Ullah, S.; Yuan, Q. The effects of bacteria-nanoparticles interface on the antibacterial activity of green synthesized silver nanoparticles. *Microb. Pathog.* **2017**, *102*, 133–142. [[CrossRef](#)]
48. Kotresh, M.; Patil, M.; Inamdar, S. Reaction temperature based synthesis of ZnO nanoparticles using co-precipitation method: Detailed structural and optical characterization. *Optik* **2021**, *243*, 167506. [[CrossRef](#)]
49. Sher, M.; Khan, S.A.; Shahid, S.; Javed, M.; Qamar, M.A.; Chinnathambi, A.; Almoallim, H.S. Synthesis of novel ternary hybrid g-C₃N₄@ Ag-ZnO nanocomposite with Z-scheme enhanced solar light-driven methylene blue degradation and antibacterial activities. *J. Environ. Chem. Eng.* **2021**, *9*, 105366. [[CrossRef](#)]
50. Jourshabani, M.; Shariatnia, Z.; Badiie, A. Facile one-pot synthesis of cerium oxide/sulfur-doped graphitic carbon nitride (g-C₃N₄) as efficient nanophotocatalysts under visible light irradiation. *J. Colloid Interface Sci.* **2017**, *507*, 59–73. [[CrossRef](#)]
51. Kalisamy, P.; Lallimathi, M.; Suryamathi, M.; Palanivel, B.; Venkatachalam, M. ZnO-embedded S-doped g-C₃N₄ heterojunction: Mediator-free Z-scheme mechanism for enhanced charge separation and photocatalytic degradation. *RSC Adv.* **2020**, *10*, 28365–28375. [[CrossRef](#)]
52. Norouzzadeh, P.; Golzan, M.; Mabhouti, K.; Naderali, R. Effect of Mn-substitution on impedance spectroscopy and magnetic properties of Al-doped ZnO nanoparticles. *Nanotechnology* **2020**, *31*, 325704. [[CrossRef](#)]
53. Rana, A.K.; Kumar, Y.; Rajput, P.; Jha, S.N.; Bhattacharyya, D.; Shirage, P.M. Search for origin of room temperature ferromagnetism properties in Ni-doped ZnO nanostructure. *ACS Appl. Mater. Interfaces* **2017**, *9*, 7691–7700. [[CrossRef](#)]
54. Simmons, E. Reflectance spectroscopy: Application of the Kubelka-Munk theory to the rates of photoprocesses of powders. *Appl. Opt.* **1976**, *15*, 951–954. [[CrossRef](#)] [[PubMed](#)]
55. Luu Thi, L.A.; Neto, M.M.; Van, T.P.; Nguyen Ngoc, T.; Nguyen Thi, T.M.; Nguyen, X.S.; Nguyen, C.T. In Situ g-C₃N₄@ ZnO Nanocomposite: One-Pot Hydrothermal Synthesis and Photocatalytic Performance under Visible Light Irradiation. *Adv. Mater. Sci. Eng.* **2021**, *2021*, 6651633. [[CrossRef](#)]
56. Rosli, N.I.M.; Lam, S.-M.; Sin, J.-C.; Satoshi, I.; Mohamed, A.R. Photocatalytic performance of ZnO/g-C₃N₄ for removal of phenol under simulated sunlight irradiation. *J. Environ. Eng.* **2018**, *144*, 04017091. [[CrossRef](#)]
57. Mohamed, R.; Shawky, A. CNT supported Mn-doped ZnO nanoparticles: Simple synthesis and improved photocatalytic activity for degradation of malachite green dye under visible light. *Appl. Nanosci.* **2018**, *8*, 1179–1188. [[CrossRef](#)]
58. Labhane, P.; Patle, L.; Sonawane, G.; Sonawane, S. Fabrication of ternary Mn doped ZnO nanoparticles grafted on reduced graphene oxide (RGO) sheet as an efficient solar light driven photocatalyst. *Chem. Phys. Lett.* **2018**, *710*, 70–77. [[CrossRef](#)]
59. Paul, D.R.; Sharma, R.; Panchal, P.; Malik, R.; Sharma, A.; Tomer, V.K.; Nehra, S. Silver doped graphitic carbon nitride for the enhanced photocatalytic activity towards organic dyes. *J. Nanosci. Nanotechnol.* **2019**, *19*, 5241–5248. [[CrossRef](#)]
60. Sun, J.-X.; Yuan, Y.-P.; Qiu, L.-G.; Jiang, X.; Xie, A.-J.; Shen, Y.-H.; Zhu, J.-F. Fabrication of composite photocatalyst g-C₃N₄-ZnO and enhancement of photocatalytic activity under visible light. *Dalton Trans.* **2012**, *41*, 6756–6763. [[CrossRef](#)]
61. Farouq, R. Coupling Adsorption-Photocatalytic Degradation of Methylene Blue and Maxilon Red. *J. Fluoresc.* **2022**, *32*, 1381–1388. [[CrossRef](#)]

62. Iqbala, S.; Iqbala, M.; Sibtaina, A.; Iqbal, A.; Farooqic, Z.H.; Ahmadd, S.; Mustafaa, K.; Musaddiqa, S. Solar driven photocatalytic degradation of organic pollutants via Bi. *Desalin. Water Treat.* **2021**, *216*, 140–150. [[CrossRef](#)]
63. Sobahi, T.R.; Amin, M. Synthesis of ZnO/ZnFe₂O₄/Pt nanoparticles heterojunction photocatalysts with superior photocatalytic activity. *Ceram. Int.* **2020**, *46*, 3558–3564. [[CrossRef](#)]
64. Falak, P.; Hassanzadeh-Tabrizi, S.; Saffar-Teluri, A. Synthesis, characterization, and magnetic properties of ZnO-ZnFe₂O₄ nanoparticles with high photocatalytic activity. *J. Magn. Magn. Mater.* **2017**, *441*, 98–104. [[CrossRef](#)]
65. Jaffari, Z.H.; Lam, S.-M.; Sin, J.-C.; Zeng, H.; Mohamed, A.R. Magnetically recoverable Pd-loaded BiFeO₃ microcomposite with enhanced visible light photocatalytic performance for pollutant, bacterial and fungal elimination. *Sep. Purif. Technol.* **2020**, *236*, 116195. [[CrossRef](#)]
66. Wu, Z.; Chen, X.; Liu, X.; Yang, X.; Yang, Y. A ternary magnetic recyclable ZnO/Fe₃O₄/g-C₃N₄ composite photocatalyst for efficient photodegradation of monoazo dye. *Nanoscale Res. Lett.* **2019**, *14*, 147. [[CrossRef](#)]
67. Kulkarni, S.D.; Kumbar, S.; Menon, S.G.; Choudhari, K.; Santhosh, C. Magnetically separable core-shell ZnFe₂O₄@ ZnO nanoparticles for visible light photodegradation of methyl orange. *Mater. Res. Bull.* **2016**, *77*, 70–77. [[CrossRef](#)]
68. Kumaresan, N.; Sinthiya, M.M.A.; Kumar, M.P.; Ravichandran, S.; Babu, R.R.; Sethurman, K.; Ramamurthi, K. Investigation on the g-C₃N₄ encapsulated ZnO nanorods heterojunction coupled with GO for effective photocatalytic activity under visible light irradiation. *Arab. J. Chem.* **2020**, *13*, 2826–2843. [[CrossRef](#)]
69. Anitha, S.; Muthukumaran, S. Microstructure, crystallographic and photoluminescence examination of Ni doped ZnO nanoparticles co-doped with Co by sol-gel method. *J. Mater. Sci. Mater. Electron.* **2017**, *28*, 12995–13005. [[CrossRef](#)]
70. Shi, Y.; Li, L.; Xu, Z.; Sun, H.; Amin, S.; Guo, F.; Shi, W.; Li, Y. Engineering of 2D/3D architectures type II heterojunction with high-crystalline g-C₃N₄ nanosheets on yolk-shell ZnFe₂O₄ for enhanced photocatalytic tetracycline degradation. *Mater. Res. Bull.* **2022**, *150*, 111789. [[CrossRef](#)]
71. Wu, Y.; Wang, Y.; Di, A.; Yang, X.; Chen, G. Enhanced photocatalytic performance of hierarchical ZnFe₂O₄/g-C₃N₄ heterojunction composite microspheres. *Catal. Lett.* **2018**, *148*, 2179–2189. [[CrossRef](#)]